Supraparamagnetic, Conductive, and Processable Multifunctional Graphene Nanosheets Coated with High-Density Fe_3O_4 Nanoparticles

Hongkun He and Chao Gao*

MOE Key Laboratory of Macromolecular Synthesis and Functionalization, Department of Polymer Science and Engineering, Zhejiang University, 38 Zheda Road, Hangzhou 310027, P. R. China

ABSTRACT The amazing properties of graphene are triggering extensive interests of both scientists and engineers, whereas how to fully utilize the unique attributes of graphene to construct novel graphene-based composites with tailor-made, integrated functions remains to be a challenge. Here, we report a facile approach to multifunctional iron oxide nanoparticle-attached graphene nanosheets (graphene@Fe_3O_4) which show the integrated properties of strong supraparamagnetism, electrical conductivity, highly chemical reactivity, good solubility, and excellent processability. The synthesis method is efficient, scalable, green, and controllable and has the feature of reduction of graphene oxide and formation of Fe_3O_4 nanoparticles in one step. When the feed ratios are adjusted, the average diameter of Fe_3O_4 nanoparticles (1.2−6.3 nm), the coverage density of Fe_3O_4 nanoparticles on graphene nanosheets (5.3−57.9%), and the saturated magnetization of graphene@Fe_3O_4 (0.5−44.1 emu/g) can be controlled readily. Because of the good solubility of the as-prepared graphene@Fe_3O_4, highly flexible and multifunctional films composed of polyurethane and a high content of graphene@Fe_3O_4 (up to 60 wt %) were fabricated by the solution-processing technique. The graphene@Fe_3O_4 hybrid sheets showed electrical conductivity of 0.7 S/m and can be aligned into a layered-stacking pattern in an external magnetic field. The versatile graphene@Fe_3O_4 nanosheets hold great promise in a wide range of fields, including magnetic resonance imaging, electromagnetic interference shielding, microwave absorbing, and so forth.

KEYWORDS: graphene • magnetite • conductivity • nanoparticles • magnetism

1. INTRODUCTION

Graphene has been receiving great attention recently due to its unprecedented combination of unique electrical, mechanical, thermal, and optical properties within a single sheet of sp^2-bonded carbon atoms (1–6). With the unique two-dimensional (2D) platelike structure and the very high specific surface area (2630 m^2/g) (7), graphene could serve as an ideal substrate for the deposition of inorganic nanoparticles (NPs) (8–16). For example, Mülhaupt et al. (8) loaded Pd NPs on graphene nanosheets and applied them as catalysts to the Suzuki-Miyaura coupling reaction. Cao et al. (14) used graphene as an electron-transport matrix to synthesize the graphene-CdS quantum dot nanocomposite and detected a picosecond ultrafast electron transfer process from the excited CdS to graphene by time-resolved fluorescence spectroscopy.

In this regard, magnetic iron oxide (e.g., maghemite γ-Fe_2O_3 or magnetite Fe_3O_4) NPs have been brought into sharp focus largely due to their magnetic properties, low toxicity, and biocompatibility in physiological environments. Decorating magnetic iron oxide NPs on graphene will impart the desirable magnetic property into graphene, making the composite promising for a variety of fields such as biomedicine, magnetic energy storage, magnetic fluids, catalysis, and environmental remediation (15, 16). Chen et al. (17) deposited Fe_3O_4 NPs onto graphene oxide (GO) by a chemical precipitation method and investigated the binding of the anticancer drug doxorubicin hydrochloride (DXR) on the hybrid for controlled targeted drug delivery. Yu et al. (18) decorated reduced GO sheets with Fe_3O_4 NPs by high-temperature decomposition of the precursor iron(III) acetylacetonate ($Fe(acac)_3$) and proposed their use as a magnetic resonance contrast agent. Fan et al. (19) reported the attachment of surface-modified Fe_3O_4 NPs to GO by covalent bonding. Ye and co-workers (20) prepared GO loaded with both γ-Fe_2O_3 and Fe_3O_4−NPs using $Fe(acac)_3$ in 1-methyl-2-pyrrolidone (NMP) at 190 °C, while Kumar et al. (21) obtained α- and γ-Fe_2O_3 NPs-deposited GO composites at ∼150 °C.

Despite the significant efforts, there exist some challenges and problems in the field of graphene/NPs composites: (1) the integrated properties of both graphene and NPs were rarely concerned, (2) the solubility/dispersibility of functionalized graphene nanosheets needs to be improved since the atomic force microscopy (AFM) image of single hybrid sheets has been scarcely reported yet, (3) the composites have rare functional groups for further chemical modification, (4) the preparation protocol is relatively complex, and (5) both size and coverage density of NPs on graphene were hardly controlled.

* Corresponding author. E-mail: chaogao@zju.edu.cn.
Received for review July 29, 2010 and accepted October 4, 2010
DOI: 10.1021/am100673g

To resolve such problems, here, we show multifunctional graphene nanosheets attached with magnetite NPs (graphene@Fe_3O_4) that integrate both the electrically conductive property of graphene and the superparamagnetism of Fe_3O_4 NPs through a facile strategy. Compared with the previous reports, our work shows various advantages. First, the synthesis method of graphene@Fe_3O_4 is simple since the reduction of GO to graphene and the in situ formation of Fe_3O_4 NPs on graphene sheets are accomplished in a one-step reaction. Second, the surfaces of graphene are evenly covered with uniform Fe_3O_4 crystal NPs, and the NPs deposited on graphene sheets are noticeably dense. Third, the growth process of Fe_3O_4 NPs on graphene sheets has been traced by transmission electron microscopy (TEM) and AFM observations, showing the mechanism for the dense coverage of NPs on graphene sheets. Fourth, the multifunctional graphene@Fe_3O_4 composites possess both the electrically conductive and superparamagnetic properties, and they have good dispersibility in polar solvents and are feasible for solution processing. The combined properties of graphene@Fe_3O_4 hold great promise in a wide range of fields, including magnetic separation, biological imaging, aligned substrate for nanodevices, electromagnetic materials and coatings, conducting polymer nanocomposites, and so forth.

2. EXPERIMENTAL SECTION

Materials. Anhydrous iron(III) chloride ($FeCl_3$, 98%) and diethylene glycol (DEG, 99%) were purchased from Alfa Aesar and used as received. Graphite powder (40 μm) was obtained from Qingdao Henglide Graphite Co., Ltd. Iron(III) acetylacetonate ($Fe(acac)_3$, Acros, 99%) and palmitoyl chloride (Fluke, 97%) were used as received. NaOH, *N,N*-dimethyl formamide (DMF), and other organic reagents or solvents were obtained from Sinopharm Chemical Reagent Co., Ltd. and used as received.

Instruments. Transmission electron microscopy (TEM) analysis was performed on a FEI/Philips CM200 electron microscope operating at 160 kV or a FEI Tecnai G2 F30 S-Twin electron microscope operating at 300 kV. Scanning electron microscopy (SEM) images were obtained on a Hitachi S4800 field-emission SEM system. Atomic force microscopy (AFM) measurements were done using a Digital Instrument Nanoscope IIIa scanning probe microscope, operating at the tapping mode, with samples prepared by spin-coating sample solutions onto freshly cleaved mica substrates at 1500 rpm. The X-ray diffractions (XRD) were recorded on a Philips X'Pert PRO diffractometer equipped with Cu Kα radiation (40 kV, 40 mA). X-ray photoelectron spectroscopy (XPS) measurements were performed with a RBD upgraded PHI-5000C ESCA system (Perkin-Elmer) with Mg Kα radiation ($h\nu = 1253.6$ eV) at a power of 250 W. Near-edge X-ray absorption fine structure (NEXAFS) spectroscopy characterizations were performed at the BL08U beamline of Shanghai Synchrotron Radiation Facility (SSRF). Raman spectra were collected on a Jobin-Yvon LabRam HR 800 Raman spectroscope equipped with a 514.5 nm laser source. The magnetic properties were measured using a sample-vibrating magnetometer (VSM, Lake Shore 7410). Thermal gravimetric analysis (TGA) was carried out on a Perkin-Elmer Pyris 6 TGA instrument with a heating rate of 20 °C/min under a nitrogen flow (30 mL/min). Fourier-transform infrared (FTIR) spectra were recorded on a Bruker Vector 22 spectrometer (KBr disk). The electrical conductivities of samples were measured using a Broadband Dielectric spectrometer (Novocontrol Turnkey Concept N40).

Preparation of GO. GO was synthesized from natural graphite powder according to the previous resports (22–24), using a modified Hummers method (25, 26) that was originally developed by Kovtyukhova et al. (27). The synthesis procedure consisted of two steps of oxidation. In the first preoxidation step, concentrated H_2SO_4 (80 mL) was added into a 500 mL round-bottom flask and heated to 80 °C. $K_2S_2O_8$ (16.8 g) and P_2O_5 (16.8 g) were added successively under magnetic stirring. Graphite powder (20 g) was then added slowly into the above solution. The mixture was kept at 80 °C for 4.5 h. After cooling down to room temperature, the mixture was diluted with deionized water and left overnight. Then, the mixture was vacuum-filtered and washed with deionized water (3.2 L) using a 0.22 μm polycarbonate membrane. The solid was dried under ambient condition for 1 day or longer. In the second oxidation step, a 1 L three-necked round-bottom flask containing 460 mL of concentrated H_2SO_4 was chilled to 0 °C in an ethanol-circulated refrigerator equipped with a magnetic stirrer. The preoxidized graphite powder was put into the flask and stirred. Then, $KMnO_4$ (60 g) was added very slowly under continuous stirring, and the temperature was kept below 10 °C. (*Caution*: quickly adding $KMnO_4$ into concentrated H_2SO_4 with poor stirring and bad heat transfer may result in highly explosive manganese (VII) oxide.) The mixture was then placed in a water bath at 35 °C and stirred for 2 h. The mixture was then diluted with deionized water (0.92 L) and stirred for 2 h in the ethanol-circulated refrigerator to keep the temperature below 50 °C. Successively, an additional 2.8 L of deionized water was added, followed by addition of 30% H_2O_2 (50 mL), causing the color of the mixture to change to bright yellow. The mixture was left undisturbed for 4 days or longer after which the nearly clear supernatant was decanted. The precipitate mixture was put into several 50 mL plastic centrifuge tubes and centrifuged and then washed successively with 1 M HCl solution (at least three centrifugation cycles, centrifugation condition: 10 000 rpm for 3 min) and deionized water (at least five centrifugation cycles, centrifugation condition: 17 500 rpm for longer than 5 min) until the decantate became neutral. The resulting product (GO) was finally stored in deionized water without drying. To determine the concentration of GO in the GO aqueous solution, a certain amount of GO solution was taken and separated by centrifugation, washed with acetone thrice, dried under vacuum at 60 °C overnight, and weighed.

Preparation of Graphene@Fe_3O_4. Typically, NaOH (200 mg) was added into DEG (20 mL), heated at 120 °C for 1 h in a nitrogen atmosphere, and cooled down to 70 °C to produce a NaOH/DEG stock solution (10 mg NaOH/mL). GO (30 mg) was separated by centrifugation from GO aqueous solution (16 000 rpm, 5 min), redispersed in DEG (20 mL), and sonicated for 1 h. Then, $FeCl_3$ (120 mg) was added and stirred for 1 h. The above mixture was heated to 220 °C for 30 min under the protection of nitrogen flow and constant stirring. A 70 °C NaOH/DEG stock solution (5 mL) was injected rapidly into the above hot mixture. The resulting mixture was further heated at 220 °C for 1 h. The final product of graphene@Fe_3O_4 (conditions: the mass feed ratio of $FeCl_3$ to GO (R_{feed}-$FeCl_3$) is 4, the mass feed ratio of NaOH to GO (R_{feed}-NaOH) is 5/3, the reaction time after addition of NaOH/DEG stock solution is 1 h) was separated by centrifugation and washed with ethanol. The experimental data of different feed ratios are given in Table 1.

Preparation of Graphene@Fe_3O_4–C_{16}. Graphene@Fe_3O_4 (2 mg) was dispersed via sonication in 8 mL of dried DMF. After dried triethylamine (0.35 g) and palmitoyl chloride (0.3 g) were added, the reaction was allowed to proceed at 60 °C for 24 h. The product of graphene@Fe_3O_4–C_{16} was isolated by centrifugation and rinsed with 1 M HCl, deionized water, and acetone.

MR Imaging. Magnetic resonance imaging (MRI) tests were performed on a 1.5 T clinical MRI instrument with a surface coil (Signa Excite HDe, GE Health Care, Milwaukee, WI). Graphene@

Table 1. Selected Reaction Conditions with Reaction Time of 1 h and Results for the Synthesis of Graphene@Fe_3O_4 Hybrid Nanosheets

R_{feed}-$FeCl_3$	R_{feed}-NaOH	GO (mg)	$FeCl_3$ (mg)	NaOH (mg)	D (nm)[a]	C (%)[b]	M_s (emu/g)[c]
0.5	5/3	30	15	50	5.2	13.9	0.7
1	5/3	30	30	50	5.4	24.6	5.7
2	5/3	30	60	50	6.2	35.2	30.7
3	5/3	30	90	50	6.3	47.2	44.1
4	5/3	30	120	50	6.3	57.9	42.8
2	1/3	30	60	10	1.2	5.3	0.5
2	1	30	60	30	5.9	24.7	25.0
2	3	30	60	90	6.3	37.0	41.0

[a] The average diameter of Fe_3O_4 nanoparticles attached on graphene sheets. [b] The coverage density of Fe_3O_4 nanoparticles on graphene nanosheets (calculated from the ratio of the projective area of nanoparticles on graphene to the area of graphene of corresponding TEM images). [c] The saturated magnetization of the graphene@Fe_3O_4.

Fe_3O_4 powders (or GO, etc.) were dispersed in a 1% aqueous solution of agarose with various concentrations and then poured into 24-well culture plates (Costar 3524, Corning Inc.) at a volume of 3 mL per well. Agarose was allowed to gel at room temperature. The spaces surrounding each well were full of deionized water to allow appropriate image acquisition. A T_2-weighted map was acquired using a spin−echo imaging sequence (TR = 2000 ms; TE = 30, 60, 90, and 120 ms; acquisition matrix = 256 × 256; field of view = 18 × 18 cm; slice thickness = 6 mm; number of averages = 1) (28).

Preparation of Graphene@Fe_3O_4/Polyurethane Composites. Polyurethane was dissolved in DMF to form a 125 mg/mL polyurethane/DMF solution. A certain amount of graphene@Fe_3O_4 was dispersed in DMF by sonication and mixed with the polyurethane/DMF solution. The mixture was then spread onto a piece of glass, dried in an oven at 60 °C for 48 h, and cooled down to room temperature. The glass was immersed into deionized water to allow the strip to peel off the glass. The strip was clamped between two filtered papers and dried in vacuum at 70 °C for 12 h.

3. RESULTS AND DISCUSSION

One-Pot Synthesis and Characterizations of Graphene@Fe_3O_4 Hybrid Nanosheets. To produce soluble graphene-based nanohybrids, graphene is seldom used as a direct starting material, since pure graphene sheets have rare surface functional moieties and poor dispersibility in solvents. Fortunately, graphene oxide (GO) has been proved to be a suitable substitute for graphene, because it possesses lots of oxygen-contained functional groups and can form homogeneous colloidal suspensions in water and polar organic solvents. Also, large-scale preparation of GO is viable by oxidation of natural graphite with strong oxidants. However, GO is electrically insulating (29) and thermally unstable (30), posing a barrier to its applications. Therefore, it is highly needed to convert GO into graphene by reduction via chemical, thermally mediated, or electrochemical methods (31). Although the reduction of GO is feasible, once GO has been incorporated into composites, it is difficult to completely reduce GO to graphene without causing any disruptions to other parts of the composites. Thus, if GO could be reduced during the synthesis process of hybrids or composites, the protocol will be greatly superior.

Generally, three approaches could be used to achieve graphene@Fe_3O_4 hybrids from GO: (1) first preparation of GO@Fe_3O_4 following reduction of the product, (2) first reduction of GO and then loading Fe_3O_4 NPs, and (3) one-pot simultaneous reduction of GO and coating Fe_3O_4 NPs. The first approach may lead to the detachment of NPs from the nanosheets due to the decomposition of organic linkers during the reduction. As mentioned above, the serious problem associated with the second approach is the aggregation of reduced graphene nanosheets, implying that it is very hard to obtain well dispersed single graphene@Fe_3O_4 sheets. Besides the poor effect, the two approaches need two pots/steps of reactions, which is adverse for the cost-effective production of the nanohybrids. Herein, we employ the thrid approach to fabricate graphene@Fe_3O_4 composites via a one-step/pot reaction through a high-temperature solution-phase hydrolysis process (32). The results demonstrated that the one-step approach is superior indeed.

Considering the green process, we selected $FeCl_3$ rather than the generally used $Fe(acac)_3$ as the raw material of iron source. In the reaction, Fe^{3+} ions were first coordinated to the surfaces of GO and then transformed into Fe_3O_4 NPs in the presence of reducing solvent of DEG with the addition of NaOH at elevated temperature, giving rise to graphene@Fe_3O_4 hybrid nanosheets. We have done various experiments with different feed ratios of $FeCl_3$ to GO (R_{feed}-$FeCl_3$), feed ratios of NaOH to GO (R_{feed}-NaOH), or reaction time (t) for the synthesis of graphene@Fe_3O_4. The products have been characterized adequately with various techniques shown below.

As seen in the representative TEM images of graphene@Fe_3O_4 (Figure 1a−c), the surfaces of graphene are densely covered by narrowly distributed Fe_3O_4 NPs with average size of 6.3 nm (Figure 1d). The distribution of Fe_3O_4 NPs on each graphene sheet is even, and no big conglomeration of Fe_3O_4 NPs or large vacancy on graphene is observed. The lattice fringe spacing (0.25 nm) displayed in the high resolution transmission electron microscopy (HRTEM) image (the inset in Figure 1c) agrees well with the lattice spacing of (311) planes of cubic magnetite.

Figure 2 shows the typical AFM images of single sheets of graphene@Fe_3O_4 with lateral dimensions of several micrometers. The flat surface of graphene is continuously dotted with protrudent particles without obvious lacuna and has an average thickness of 10−20 nm, which results from

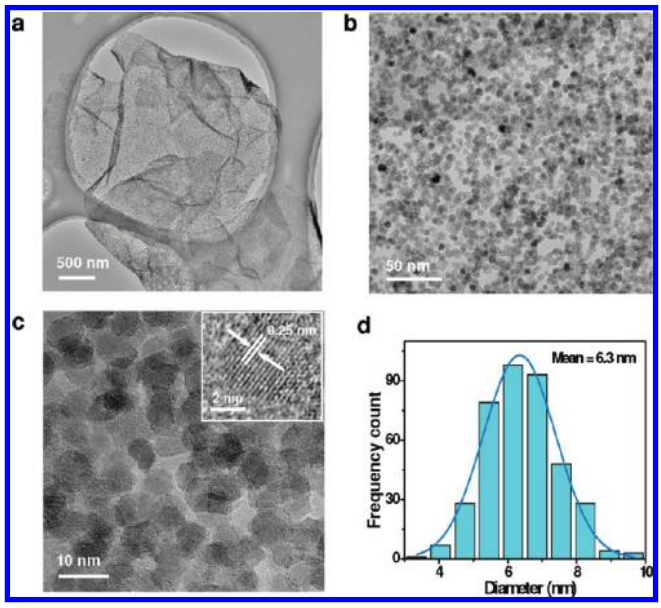

FIGURE 1. TEM images at increasing magnification (a−c) and size distribution analysis of Fe_3O_4 nanoparticles (d) of graphene@Fe_3O_4 (R_{feed}-$FeCl_3$ = 4, R_{feed}-NaOH = 5/3, and t = 1 h).

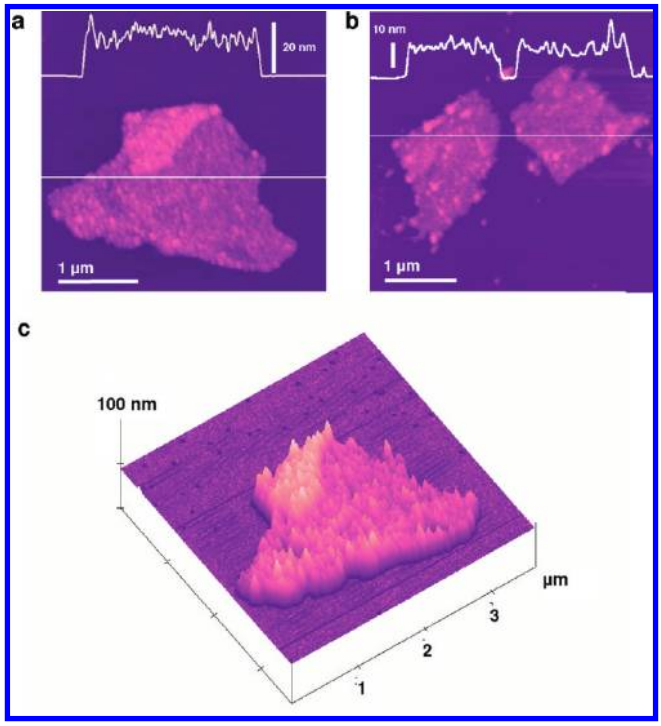

FIGURE 2. AFM images (a, c) of graphene@Fe_3O_4 (R_{feed}-$FeCl_3$ = 4, R_{feed}-NaOH = 5/3, and t = 1 h), and AFM image (b) of graphene@Fe_3O_4 (R_{feed}-$FeCl_3$ = 2, R_{feed}-NaOH = 5/3, t = 15 min).

the fact that both sides of each graphene sheet are coated with Fe_3O_4 NPs. AFM images of other graphene@Fe_3O_4 samples with different feed ratio or reaction time (see the Supporting Information, Figure S4) show mostly single sheets, suggesting the individual graphene sheets remain isolated after being loaded with Fe_3O_4 NPs.

The scanning electron microscopy (SEM) measurements show the thick cakes of graphite (Figure 3a) have been exfoliated into thin large flakes of GO (Figure 3b) after oxidation. In the SEM images of graphene@Fe_3O_4 with various feed ratios (Figure 3c−e), the Fe_3O_4 NPs appear as

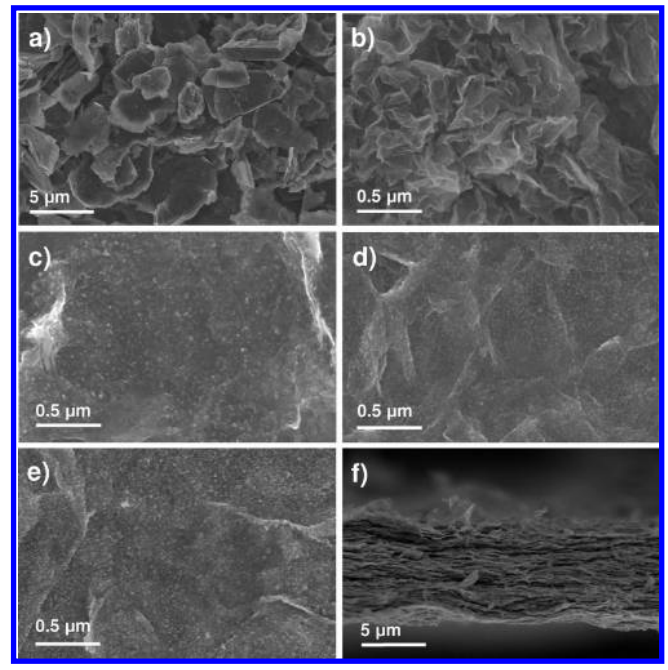

FIGURE 3. SEM top-view images of graphite (a), GO (b), graphene@Fe_3O_4 with different R_{feed}-$FeCl_3$ (t = 1 h, R_{feed}-NaOH = 5/3, R_{feed}-$FeCl_3$ = 2 (c), 3 (d), and 4 (e)), and SEM side-view image of a filtered sample of graphene@Fe_3O_4 (f).

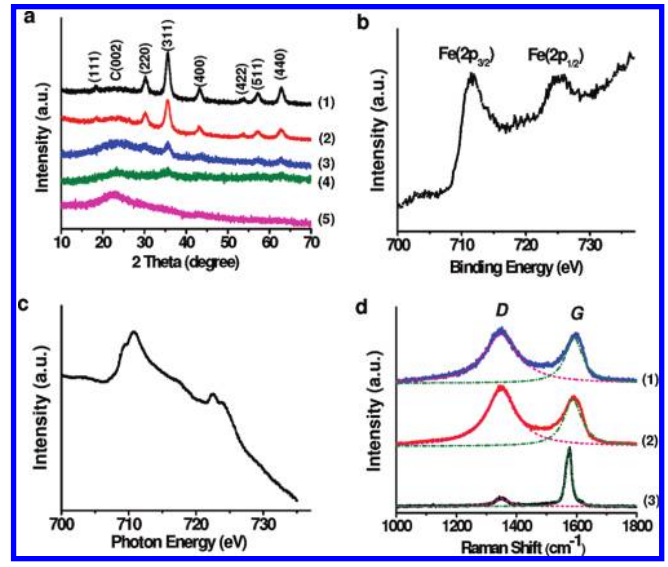

FIGURE 4. (a) XRD patterns of graphene@Fe_3O_4 with R_{feed}-$FeCl_3$ = 4 (1), 3 (2), 2 (3), 1 (4), and 0.5 (5). (b) The Fe 2p high resolution XPS spectrum of graphene@Fe_3O_4. (c) NEXAFS spectrum at Fe L edges of graphene@Fe_3O_4. (d) Raman spectra of graphene@Fe_3O_4 (1), GO (2), and graphite (3).

bright dots, and the large graphene flakes exhibit a slightly wrinkled surface. The side-view SEM image (Figure 3f) of the cross-sectioned edge of a vacuum filtered graphene@Fe_3O_4 film shows a layered structure of thin graphene sheets.

The crystalline structure of Fe_3O_4 NPs on graphene was corroborated by XRD measurements. As seen in Figure 4a, the pattern of graphene@Fe_3O_4 displayed obvious diffraction peaks of Fe_3O_4, and the peak positions and relative intensities match well with the standard XRD data for magnetite (JCPDS card, file No. 19-0629). The broad diffraction peak around 23° corresponds to C(002) reflection of

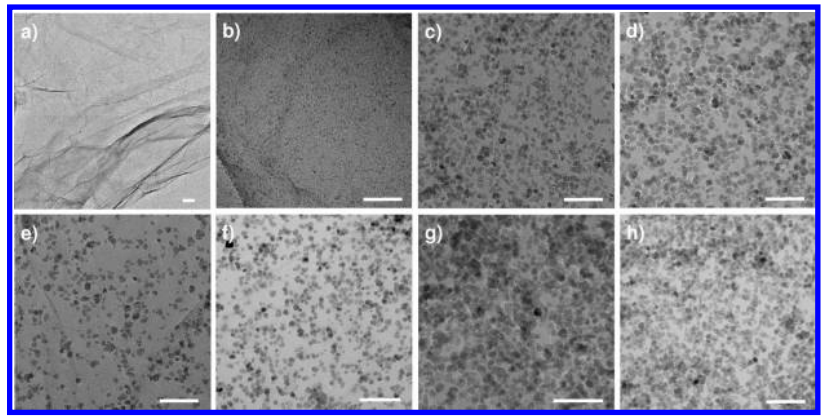

FIGURE 5. TEM images of GO (a), graphene@Fe_3O_4 with different R_{feed}-NaOH (t = 1 h, R_{feed}-$FeCl_3$ = 2, R_{feed}-NaOH = 1/3 (b), 1 (c), and 3 (d)), and graphene@Fe_3O_4 with different R_{feed}-$FeCl_3$ (t = 1 h, R_{feed}-NaOH = 5/3, R_{feed}-$FeCl_3$ = 0.5 (e), 1 (f), 2 (g), and 3 (h)). Scale bars, 50 nm.

graphite derived from the short-range order in stacked graphene sheets (12), indicating the reduction of GO in the reaction process (33). With the enlarging of R_{feed}-$FeCl_3$, the intensity of Fe_3O_4 diffraction peaks become more and more distinct, due to the increasing coverage of Fe_3O_4 NPs on graphene. Simultaneously, the C(002) peak gets weakened gradually and cannot be detected for the sample with R_{feed}-$FeCl_3$ = 4, indicating that the reduced graphene sheets cannot stack with each other any more to form crystalline structures if the coverage of NPs is densely enough. In other words, individually separated graphene@Fe_3O_4 sheets can be obtained in both suspensions and solids.

The X-ray photoelectron spectroscopy (XPS) and near-edge X-ray absorption fine structure (NEXAFS) spectrum were used to further identify the crystal phase of Fe_3O_4. In the Fe 2p high resolution XPS spectrum of graphene@Fe_3O_4 (Figure 4b), the binding energy peaks at 711.7 and 725.3 eV are corresponding to Fe $2p_{3/2}$ and Fe $2p_{1/2}$, respectively, which are very close to the values of Fe_3O_4 published in the literature (34). It is noteworthy that the charge transfer satellite of Fe $2p_{3/2}$ was not detected at around 720 eV, revealing the formation of mixed oxides of Fe(II) and Fe(III) such as Fe_3O_4 (35). In the NEXAFS spectrum at the Fe L absorption edges, the splitting of the L_3 peak in the region of 705−710 eV and the ratio of two peaks at the L_2 edge (719−725 eV) are two important features for distinguishing between Fe_3O_4, γ-Fe_2O_3, and α-Fe_2O_3. For the L_3 peak in the region of 705−710 eV in Figure 4c, the splitting was measured to be 1.28 eV, which is close to the value reported in the literature for Fe_3O_4 (36). For the two peaks at the L_2 edge (719−725 eV) in Figure 4c, the left peak is relatively stronger than the right one, which agrees well with the case reported in the literature for Fe_3O_4 (37).

The Raman spectra of graphite, GO, and graphene@Fe_3O_4 (Figure 4d) provide the information about the structural changes during the chemical reactions. The G band around 1580 cm^{-1} is related to the in-plane vibration of sp^2 carbon atoms in a 2D hexagonal lattice, and the D band around 1350 cm^{-1} is assigned to the vibrations of sp^3 carbon atoms of disordered graphite (38). The intensity ratio of the D and G band (I_D/I_G) is a useful indicator to evaluate the ordered and disordered crystal structures of carbon. The value of I_D/I_G is 0.34 for graphite, and it increases to 2.04 for GO, indicating the introduction of many defect sites to GO by the oxidative treatment of graphite. The I_D/I_G for graphene@Fe_3O_4 further increases to 2.13 compared with that of GO, which could be attributed to more numerous but smaller sp^2 graphitic domains created upon reduction of GO (39) and the presence of some unrepaired defects (40). For comparison, the I_D/I_G values are 1.75 and 2.28 for pure reduced GO samples made by chemical reduction with hydrazine and solvothermal reduction with DEG, respectively (see the Supporting Information, Figure S5).

Influence of Feed Ratios on the Nanocrystal Growth. The above characterizations demonstrated the high efficiency of the one-pot approach. To show the controllability and flexibility of this approach, the results of the parallel experiments with different feed ratios and reaction time for the synthesis of graphene@Fe_3O_4 were compared. It was found that the amounts of $FeCl_3$ and NaOH added in the synthesis process are the two important factors that influence the average diameter (D) of Fe_3O_4 NPs, the coverage density (C) of Fe_3O_4 NPs on graphene nanosheets (calculated from the ratio of the projective area of NPs on graphene to the area of graphene of corresponding TEM images), and the saturated magnetization (M_s) of the graphene@Fe_3O_4. The TEM images of selected samples are shown in Figure 5, and the corresponding analytical data are shown in Figure 6. As shown in Figure 6a, at fixed R_{feed}-$FeCl_3$ = 2 and t = 1 h, the D, C, and M_s increase steadily with increasing R_{feed}-NaOH and reach the maximum ($D \sim 6.3$ nm, $C \sim 37.0\%$, $M_s \sim 41.0$ emu/g), because the high alkalinity caused by NaOH favors the quick nucleation and growth of Fe_3O_4 (36) (see Figure 5b,c,g,d, and Figure S2 of the Supporting Information). Figure 6c shows that at fixed R_{feed}-NaOH = 5/3 and t = 1 h, the D, C, and M_s increase upon increasing R_{feed}-$FeCl_3$ and reach the maximum ($D \sim 6.3$ nm, $C \sim 57.9\%$, $M_s \sim 44.1$ emu/g). This is likely due to that the elevated concentration of $FeCl_3$ would accelerate the generation of Fe_3O_4 on the graphene substrate and eventually approach a plateau at high R_{feed}-$FeCl_3$, which is in coincidence with the TEM observations (see Figures 1, 5e−h, and S1 of the Supporting Information).

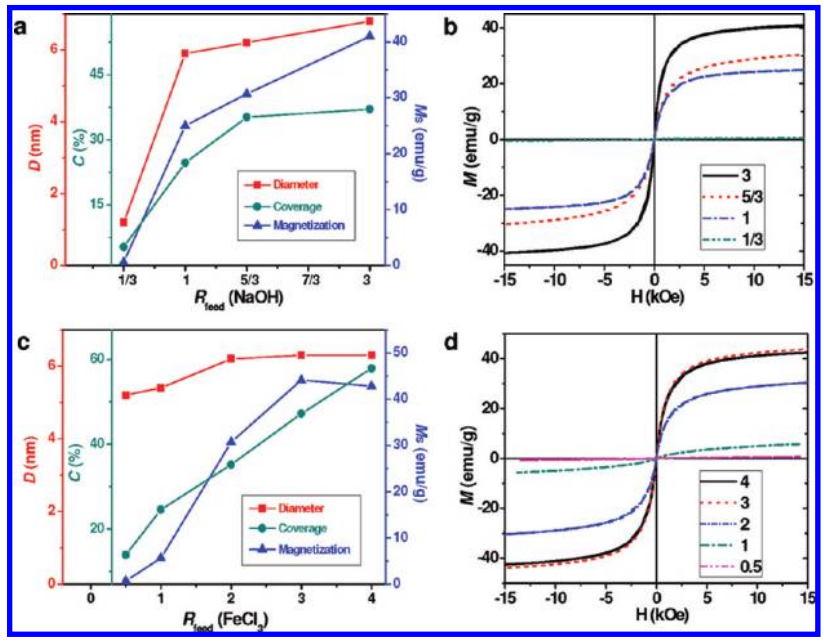

FIGURE 6. Dependence of the average diameter (D) of Fe_3O_4 nanoparticles, the coverage density (C) of Fe_3O_4 nanoparticles on graphene nanosheets, and the saturated magnetization (M_s) of graphene@Fe_3O_4 on R_{feed}-NaOH (at fixed R_{feed}-$FeCl_3$ = 2 and t = 1 h) (a) and R_{feed}-$FeCl_3$ (at fixed R_{feed}-NaOH = 5/3 and t = 1 h) (c), respectively. The corresponding magnetic hysteresis loops of (a) and (c) are shown in (b) and (d), respectively.

The obtained data are also listed in Table 1. Generally, R_{feed}-$FeCl_3$ has more significant influence on C (13.9−57.9%) than on D (5.2−6.3 nm); R_{feed}-NaOH has strong influence on both D (1.2−6.3 nm) and C (5.3−37.0%), and both R_{feed}-$FeCl_3$ and R_{feed}-NaOH have great influence on M_s (0.7−44.1 and 0.5−41.0 emu/g, respectively). It can be concluded that (1) the concentration of $FeCl_3$ primarily determines the formation of Fe_3O_4 NPs and, thus, mainly affects their coverage densities, (2) the concentration of NaOH primarily determines the growth rate of Fe_3O_4 NPs and, thus, affects their diameters and coverage densities, and (3) both the diameter and coverage density of Fe_3O_4 NPs affect the magnetizations of graphene@Fe_3O_4. The magnetic hysteresis loops of all these samples (Figure 6b,d) exhibit superparamagnetic characteristics at room temperature with no remanence or coercivity. Consequently, the synthesis strategy allows one to adjust the size of parasitical Fe_3O_4 NPs and magnetization of graphene@Fe_3O_4 readily in a wide range.

Kinetics and Mechanism of Graphene-Based Nanocrystal Growth. A proposed mechanism model for the formation of graphene@Fe_3O_4 is shown in Figure 7. With the help of the abundant surface oxygen-containing groups such as carboxyl and hydroxyl, GO is easily suspended in DEG to form a stable colloidal solution by ultrasonication. The iron precursor $FeCl_3$ was then added, and the Fe^{3+} ions were coordinated to the carboxyl groups of GO. Upon increasing the temperature to 220 °C, the color of the reaction mixture turned from light brown to dark brown and then to black, which is a sign that GO has been reduced into graphene (41). The solvothermal reduction of GO in DEG was further confirmed from the Fourier-transform infrared (FTIR) and XRD analyses of the samples obtained in the control experiment in the absence of $FeCl_3$ (see the Supporting Information, Figure S6). Upon the addition of NaOH at high temperature, Fe^{3+} ions were hydrolyzed to $Fe(OH)_3$ and then partially transformed to $Fe(OH)_2$ under the reductive surrounding and eventually dehydrated to form Fe_3O_4 NPs (36).

We traced the growth process of graphene@Fe_3O_4 by off-line TEM observations of a series of samples that are taken out from the reaction system at different times. The TEM analysis (see the inset in Figure 7 and Figure S3 of the Supporting Information) reveals that the formation of Fe_3O_4 nanocrystals on graphene was a dynamic process that follows the classic La Mer model (42). In the initial nucleation stage, a temporally discrete nucleation occurred immediately upon the rapid injection of NaOH solution. The high reaction temperature greatly accelerates the nucleation process, leading to the burst of nucleation within several seconds. The quick nucleation helps to obtain magnetite nanocrystals with relatively narrow size distributions (43). In the next growth stage, the nuclei formed in the initial stage quickly grow to larger crystals during the first 5 min after nucleation. The average particle sizes are around 1.6, 3.1, 4.0, 4.4, 4.6, and 4.8 nm at 0, 1, 2, 3, 4, and 5 min, respectively. According to the Lifshitz−Slyozov−Wagner (LSW) theory for Ostwald ripening, for a system of highly dispersed particles with the diffusion-controlled growth, the rate law is given by

$$\bar{r}^3 - \bar{r}_0^{\,3} = Kt \qquad (1)$$

$$K = \frac{8\gamma D V_m^{\,2} C_\infty}{9RT} \qquad (2)$$

where $\bar{r}$ is the mean particle radius at time t, $\bar{r}_0$ is the initial particle radius at time zero, C_∞ is the equilibrium concentra-

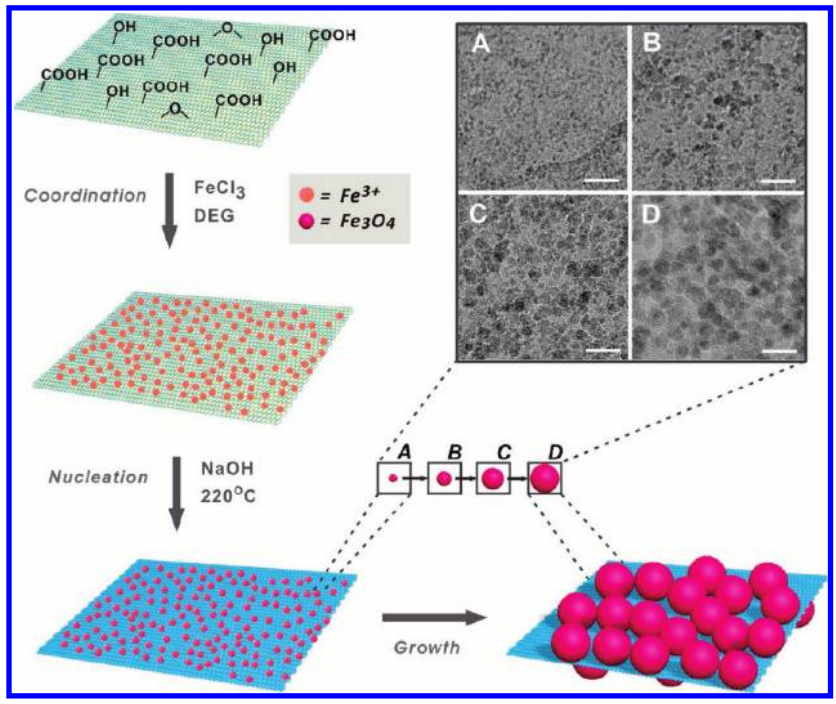

FIGURE 7. Schematic illustration of the formation of graphene@Fe_3O_4. The inset shows the TEM images of graphene@Fe_3O_4 at reaction time of 0 (A), 1 (B), 5 (C), and 60 min (D). Scale bars, 20 nm.

tion at a flat surface, γ is the interfacial energy, V_m is the molar volume of the solid phase, R is the gas constant, and T is the temperature (44). When the experimental data is fitted into eq 1 (see the inset in Figure 8a), the constant K is calculated to be 21.6 (nm^3/min). The growth kinetics of Fe_3O_4 particles follows the Ostwald ripening, in which smaller particles dissolve owing to their high surface energy and are essentially consumed by larger ones (42). After 5 min, the increase of Fe_3O_4 particle size is very slow (5.3, 5.5, 5.9, and 6.2 nm at 10, 15, 30, and 60 min, respectively), and even a 24 h of growth only leads to a particle size of 6.8 nm. The magnetic hysteresis loops of the samples obtained at different reaction times (Figure 8b) show superparamagnetic behaviors, and the change of M_s (Figure 8a) shows the similar tendency to that of a particle size increase, that is, fast increase within the first few minutes and very slow increase after that (approaching 36.1 emu/g at 24 h).

The NPs supported on graphene sheets reported herein are remarkablely dense compared with those in other reported cases of inorganic particles (8–16), presumably due to the different synthesis methods. In our cases, the process of high-temperature solution-phase hydrolysis allows the instantaneous nucleation and quick growth of Fe_3O_4 particles. In order to verify this supposition, we conducted control experiments to synthesize Fe_3O_4 NPs on GO via a commonly used high-temperature decomposition method using $Fe(acac)_3$ as the precursor. The formation of Fe_3O_4 NPs resulted from the decomposition of $Fe(acac)_3$ is a slow process, leading to graphene sheets relatively sparsely decorated with Fe_3O_4 NPs with coverage density of around 14.0% (see Figure 9a and Figure S7 of the Supporting Information). In addition, control experiments using highly reduced graphene oxide (HRG) (45) as the starting material were also conducted, but only very few Fe_3O_4 NPs were observed on the HRG sheets in the TEM image (Figure 9b). This is because the oxygen-containing functional groups are almost entirely removed from GO by hydrazine in the preparation of HRG, and Fe^{3+} ions could not coordinate to the surfaces of HRG sheets. The control experiments in turn affirm the necessity of the use of multifunctional GO instead of graphene or HRG as the starting material. Furthermore, it is noteworthy that the existence of carboxyl groups of GO is an essential prerequisite for the formation of Fe_3O_4 NPs on graphene sheets, which are confirmed by the following two control experiments. The chemically modified graphene containing carboxyl moiety can also produce graphene@Fe_3O_4, whereas Fe_3O_4 NPs cannot deposit on the chemically modified graphene containing hydroxyl moiety (see Figures 9c,d and S8 of the Supporting Information).

Solubility and Multifunctionality of Graphene@Fe_3O_4 Nanosheets. It is known that pure graphene and reduced GO without any modification tend to aggregate and could not disperse in most solvents due to the lack of surface moieties (46), which seriously limits their applications (47). Interestingly, our graphene@Fe_3O_4 hybrids could be dispersed by sonication in many polar solvents such as ethanol, water, and DMF (Figure 10a). Two main factors are responsible for the improved solubility of graphene@Fe_3O_4 as compared to graphene. For one thing, the deposited Fe_3O_4 NPs could prevent graphene sheets from severe aggregation during the reduction of GO. The same phenomenon was also found in the case of platinum NPs deposited on graphene (12). For another, the polyol solvent of DEG can attach to the surfaces of graphene@Fe_3O_4 as ligand of NPs after reaction, and enhance the dispersibility of product in polar solvents accordingly. The presence of DEG on graphene@Fe_3O_4 is confirmed by the thermal gravimetric analysis (TGA)

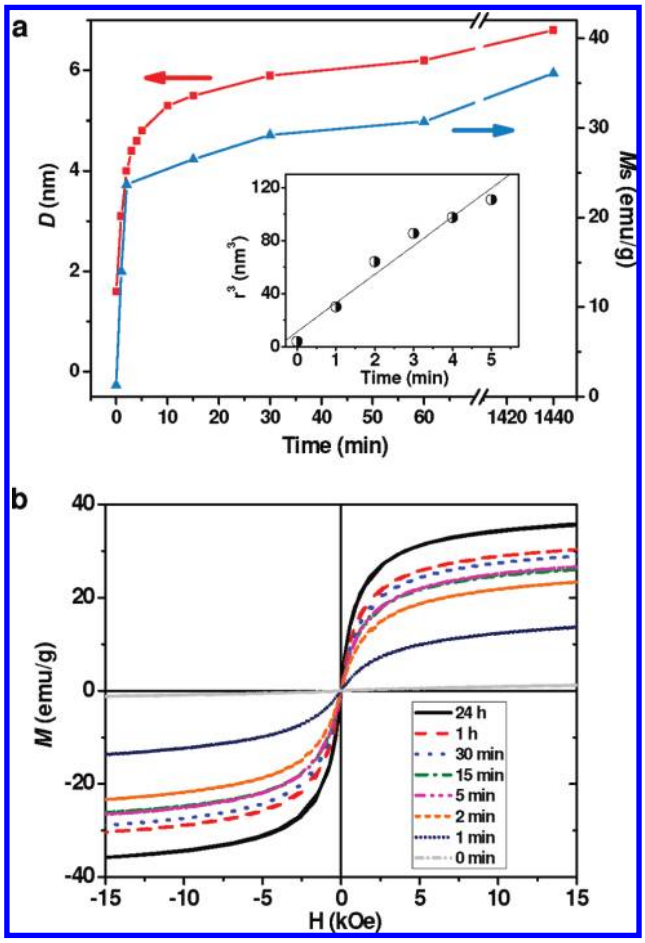

FIGURE 8. (a) Dependence of the average diameter (D) of Fe_3O_4 nanoparticles and the saturated magnetization (M_s) of graphene@Fe_3O_4 on reaction time. The inset shows the cube of average particle radius of Fe_3O_4 nanoparticles on graphene versus the growth time. The fitting line accords with the LSW model. (b) The corresponding magnetic hysteresis loops of (a).

and FTIR analyses of the graphene@Fe_3O_4 sample (see the Supporting Information, Figure S9). About 20 wt % weight loss between 230 and 500 °C was found in the TGA curve of graphene@Fe_3O_4, suggesting the high density coating of DEG on the NP surfaces. XPS measurements showed that the elemental contents of Fe, O, and C for the sample of graphene@Fe_3O_4 (t = 1 h, R_{feed}-NaOH = 5/3, R_{feed}-$FeCl_3$ = 4) were 8.66, 32.15, and 59.19%, respectively. According to the atom ratio, the Fe_3O_4 weight percent is calculated to be around 39.2%. Obviously, the extra-high oxygen content can be mainly attributed to the attachment of DEG molecules, which is in agreement with the TGA result. Such a high content of Fe_3O_4 NPs results in the strong M_ss (>40 emu/g) of our graphene@Fe_3O_4 samples. The M_s of the control sample made from $Fe(acac)_3$ is less than 10 emu/g (9.4 emu/g) due to the relatively low coverage/content of Fe_3O_4 NPs (Supporting Information Figure S7A). As a comparison, Kumar and co-workers reported that the maximum M_s of their magnetic samples made from $Fe(acac)_3$ is only 5.5 emu/g.

Furthermore, the hydroxyl groups of DEG on the graphene@Fe_3O_4 were utilized to react with palmitoyl chloride to produce long alkyl chain-modified graphene@Fe_3O_4

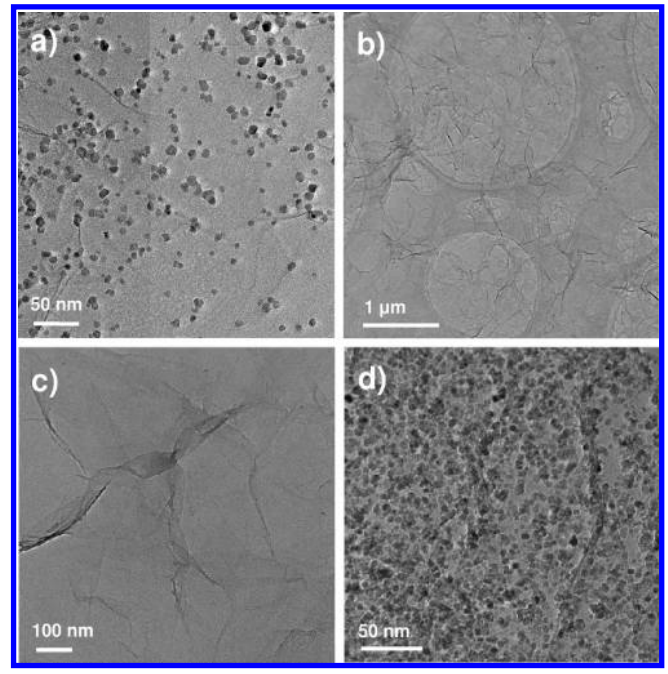

FIGURE 9. TEM images of the samples from the control experiments for graphene@Fe_3O_4: (a) using $Fe(acac)_3$ instead of $FeCl_3$/NaOH, (b) using highly reduced graphene oxide (HRG) instead of GO, (c) using chemically modified graphene with hydroxyl moiety instead of GO, and (d) using chemically modified graphene with carboxyl moiety instead of GO.

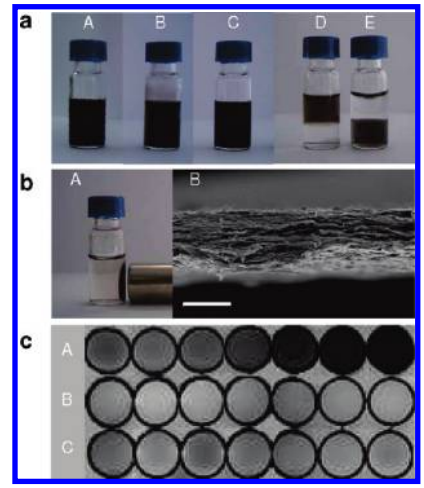

FIGURE 10. (a) Photographs of 1.5 mg/mL graphene@Fe_3O_4 dispersion in ethanol (A), water (B), and DMF (C) after sonication. The photographs of graphene@Fe_3O_4 (D) and graphene@Fe_3O_4−C_{16} (E) dispersed in water/chloroform. (b) The photograph of graphene@Fe_3O_4 in DMF separated by a magnet (A), and SEM side-view image of graphene@Fe_3O_4 dried in an external magnetic field (B). Scale bar, 5 μm. (c) T_2-weighted MR imaging of graphene@Fe_3O_4 (A), HRG (B), and GO (C) at different concentrations (from left to right in each row: 0, 6.25, 12.5, 25, 50, 100, and 200 μg/mL).

(graphene@Fe_3O_4−C_{16}), resulting in the change of surface property from hydrophilic to hydrophobic. When placed in the water/chloroform mixture, the graphene@Fe_3O_4 dispersed in the upper layer of polar water, whereas graphene@Fe_3O_4−C_{16} transferred to the lower layer of nonpolar chloroform (Figure 10a), suggesting the successful surface modification. The highly reactive platform of multihydroxyl graphene@Fe_3O_4 lays the foundation for introduc-

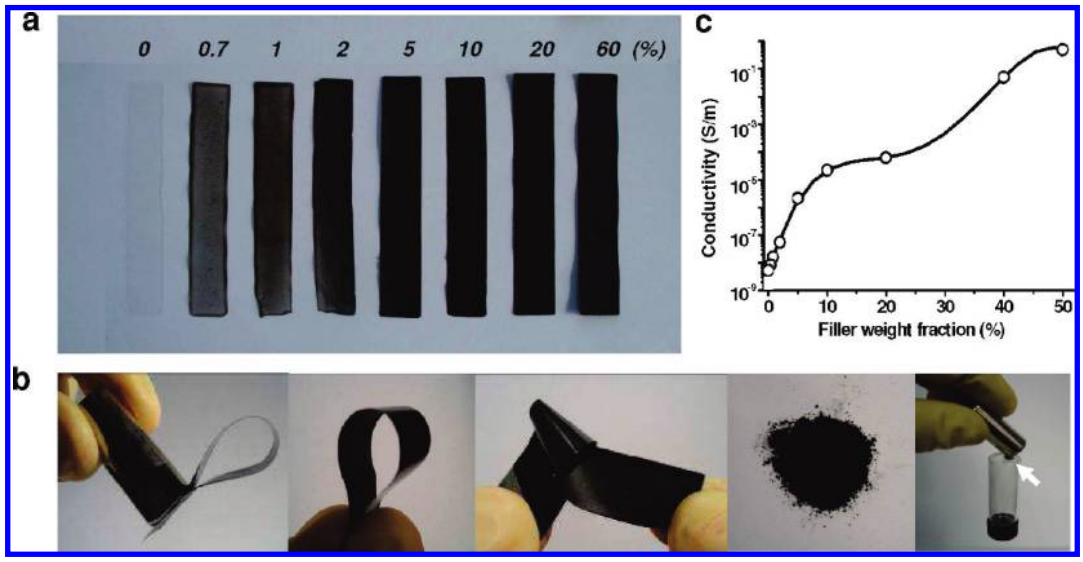

FIGURE 11. (a) Photographs of ~40 μm thick strips of graphene@Fe_3O_4–polyurethane composites with different filler contents. (b) From left to right: the photographs of a strip of graphene@Fe_3O_4–polyurethane composites (50 wt %) lifted with a magnet, held and twisted with hands, dried graphene@Fe_3O_4 powder, and 6.0 mg of graphene@Fe_3O_4 powder that can lift a 5.05 g glass bottle with a magnet, respectively. (c) Electrical conductivity of graphene@Fe_3O_4–polyurethane composites as a function of filler weight fraction.

ing other functional compositions and desired moieties with tailor-made properties by chemical modification.

Magnetic Alignment and MR Imaging. The strong superparamagnetic attribute of graphene@Fe_3O_4 offers significant use for biomagnetic separations, as the carriers for targeted drug delivery and as the contrast agents in magnetic resonance imaging (MRI). The magnetic components of graphene@Fe_3O_4 render mobility under an external magnetic field. When a magnet is placed beside a bottle filled with graphene@Fe_3O_4 dispersed in DMF, the graphene@Fe_3O_4 particles quickly move along the magnetic field and completely deposit near the magnet (Figure 10b). SEM observations on the graphene@Fe_3O_4 sheets that were separated from the solvent and dried in an external magnetic field showed an aligned layered-stacking pattern (Figure 10b), which is very similar to the vacuum-filtered samples as shown in Figure 2f. Such an example of magnetically induced self-assembly indicates that the water-soluble graphene@Fe_3O_4 could be used in the magnetic array and cell manipulation (48). This result also demonstrates that large-area aligned graphene nanosheets can be produced via magnetic force, which would be a breakthrough for the fabrication of graphene-based electromagnetic devices, transistors, and displays, as aligned carbon nanotubes have shown (49).

Moreover, since the magnetic iron oxide NPs are now established as MRI contrast agents in current MRI techniques, we also performed MRI experiments on a 1.5 T clinical imaging system to test the feasibility of the use of the superparamagnetic graphene@Fe_3O_4 as a novel contrast agent. The T_2-weight MR imaging of graphene@Fe_3O_4 shows strong MR relaxation enhancement (Figure 10c), promising its potential in MRI technology. As a comparison, no enhancement was observed for the samples containing neat GO or HRG.

Conductive and Magnetic Polymer Composites of Graphene@Fe_3O_4. The electrical conductivity is a pivotal property of graphene. Chemical treatment could improve its solubility but also may destroy the structure of graphene, usually leading to the vanishing of conductivity. Therefore, a big question appears: is the graphene@Fe_3O_4 still conductive? To our delight, the graphene@Fe_3O_4 film made by vacuum-filtering was demonstrated to be electrically conductive (~0.7 S/m). The insulative GO has been reduced to graphene via solvothermal reduction and restored the conductivity by recovering the conjugated network (40). Due to the obstruction of Fe_3O_4 NPs between the basal planes of graphene nanosheets, the conductivity of graphene@Fe_3O_4 is lower than that of HRG or modified graphene paper samples (in the range of 10^2–10^4 S/m) (45).

The solubility and versatility of the graphene@Fe_3O_4 sheets pave the way for the fabrication of multifunctional composites by the convenient solution-processing technique. Herein, we produced various graphene@Fe_3O_4-polymer films by solution-phase mixing of graphene@Fe_3O_4 with polyurethane elastomer. The colors of the resulting films turn gradually from transparent to black upon the content of graphene@Fe_3O_4 raised from 0 to 60 wt % (Figure 11a). The composite films have evident magnetic response to an external field and excellent flexibility (Figure 11b). Significantly, the film loaded with nanofillers of graphene@Fe_3O_4 as high as 50 wt % is also quite flexible and can be folded without fissuring. The electrical conductivity of the graphene@Fe_3O_4–polyurethane composites is shown in Figure 11c. The conductivity values of the graphene@Fe_3O_4–polyurethane composites are comparable with those of graphene–polymer composites reported in the literature (50). Therefore, the multifunctional graphene@Fe_3O_4 could serve as a new kind of promising nanofiller to produce high-performance polymer composites and coatings with both electrical and magnetic properties, which are greatly useful in electromagnetic interference (EMI) shielding, microwave absorbing, flexible electronics materials, etc (51, 52).

4. CONCLUSIONS

In summary, we have demonstrated a facile and efficient chemical approach to prepare multifunctional nanosheets of graphene@Fe_3O_4 with scalable, cost-effective, highly reproducible, and well controllable merits. With Fe_3O_4 NPs densely coated on the surfaces of graphene, the superparamagnetic and conductive properties are integrated into individual nanosheets, making multifunctional single-sheet nanohybrids practicable. The graphene@Fe_3O_4 nanosheets can be aligned as large-area layered-stacking films with a magnetically controlled methodology, opening the avenue to extraordinary nanoelectronic devices and materials made of graphene. The graphene@Fe_3O_4 nanocomposites are readily processable in solvents, facilitating their versatile applications. The multihydroxyl groups associated with the Fe_3O_4 NPs enable the graphene@Fe_3O_4 highly reactive, affording a 2D nanoplatform for construction of desirable bionano conjugates via a chemical approach. Our finding can be extended to different kinds of multifunctional graphene-based nanocomposites, paving the way for the extensive exploration of graphene with fascinating functionalities. In addition, because of the extremely dense coverage of Fe_3O_4 on the graphene template, the graphene@Fe_3O_4 could play the role of precursor of iron oxide nanosheets or iron oxidene, casting an optimistic light for achieving other quantum planes built with noncarbon atoms, molecules, or NPs.

Acknowledgment. This work was financially supported by the National Natural Science Foundation of China (Nos. 50773038 and 20974093), National Basic Research Program of China (973 Program; No. 2007CB936000), Qianjiang Talent Foundation of Zhejiang Province (2010R10021), the Fundamental Research Funds for the Central Universities (2009QNA4040), and the Foundation for the Author of National Excellent Doctoral Dissertation of China (No. 200527).

Supporting Information Available: Additional TEM and AFM images, Raman spectra, photographs, TGA, FTIR, and XRD data. This material is available free of charge via the Internet at http://pubs.acs.org.

REFERENCES AND NOTES

(1) Park, S.; Ruoff, R. S. *Nat. Nanotechnol.* **2009**, *4*, 217–224.
(2) Rao, C. N. R.; Sood, A. K.; Subrahmanyam, K. S.; Govindaraj, A. *Angew. Chem., Int. Ed.* **2009**, *48*, 7752–7777.
(3) Geim, A. K. *Science* **2009**, *324*, 1530–1534.
(4) Geim, A. K.; Novoselov, K. S. *Nat. Mater.* **2007**, *6*, 183–191.
(5) Katsnelson, M. I. *Mater. Today* **2007**, *10*, 20–27.
(6) Loh, K. P.; Bao, Q.; Ang, P. K.; Yang, J. *J. Mater. Chem.* **2010**, *20*, 2277.
(7) Stoller, M. D.; Park, S. J.; Zhu, Y. W.; An, J. H.; Ruoff, R. S. *Nano Lett.* **2008**, *8*, 3498–3502.
(8) Scheuermann, G. M.; Rumi, L.; Steurer, P.; Bannwarth, W.; Mülhaupt, R. *J. Am. Chem. Soc.* **2009**, *131*, 8262–8270.
(9) Muszynski, R.; Seger, B.; Kamat, P. V. *J. Phys. Chem. C* **2008**, *112*, 5263–5266.
(10) Goncalves, G.; Marques, P.; Granadeiro, C. M.; Nogueira, H. I. S.; Singh, M. K.; Gracio, J. *Chem. Mater.* **2009**, *21*, 4796–4802.
(11) Xu, C.; Wang, X.; Zhu, J. W. *J. Phys. Chem. C* **2008**, *112*, 19841–19845.
(12) Si, Y. C.; Samulski, E. T. *Chem. Mater.* **2008**, *20*, 6792–6797.
(13) Pasricha, R.; Gupta, S.; Srivastava, A. K. *Small* **2009**, *5*, 2253–2259.
(14) Cao, A.; Liu, Z.; Chu, S.; Wu, M.; Ye, Z.; Cai, Z.; Chang, Y.; Wang, S.; Gong, Q.; Liu, Y. *Adv. Mater.* **2009**, *21*, 103–106.
(15) Lu, A. H.; Salabas, E. L.; Schuth, F. *Angew. Chem., Int. Ed.* **2007**, *46*, 1222–1244.
(16) Frey, N. A.; Peng, S.; Cheng, K.; Sun, S. H. *Chem. Soc. Rev.* **2009**, *38*, 2532–2542.
(17) Yang, X. Y.; Zhang, X. Y.; Ma, Y. F.; Huang, Y.; Wang, Y. S.; Chen, Y. S. *J. Mater. Chem.* **2009**, *19*, 2710–2714.
(18) Cong, H. P.; He, J. J.; Lu, Y.; Yu, S. H. *Small* **2009**, *6*, 169–173.
(19) He, F.; Fan, J.; Ma, D.; Zhang, L.; Leung, C.; Chan, H. L. *Carbon* **2010**, *48*, 3139–3144.
(20) Shen, J. F.; Hu, Y. Z.; Shi, M.; Li, N.; Ma, H. W.; Ye, M. X. *J. Phys. Chem. C* **2010**, *114*, 1498–1503.
(21) Singh, V. K.; Patra, M. K.; Manoth, M.; Gowd, G. S.; Vadera, S. R.; Kumar, N. *New Carbon Mater.* **2009**, *24*, 147–152.
(22) Xu, Z.; Gao, C. *Macromolecules* **2010**, *43*, 6716–6723.
(23) He, H. K.; Gao, C. *Chem. Mater.* **2010**, *22*, 5054–5064.
(24) Kou, L.; He, H. K.; Gao, C. *Nano-Micro Lett.* **2010**, *2*, 177–183.
(25) Tung, V. C.; Allen, M. J.; Yang, Y.; Kaner, R. B. *Nat. Nanotechnol.* **2009**, *4*, 25–29.
(26) Hummers, W. S.; Offeman, R. E. *J. Am. Chem. Soc.* **1958**, *80*, 1339–1339.
(27) Kovtyukhova, N. I.; Ollivier, P. J.; Martin, B. R.; Mallouk, T. E.; Chizhik, S. A.; Buzaneva, E. V.; Gorchinskiy, A. D. *Chem. Mater.* **1999**, *11*, 771–778.
(28) Wan, J.; Cai, W.; Meng, X.; Liu, E. *Chem. Commun.* **2007**, 5004–5006.
(29) Jung, I.; Pelton, M.; Piner, R.; Dikin, D. A.; Stankovich, S.; Watcharotone, S.; Hausner, M.; Ruoff, R. S. *Nano Lett.* **2007**, *7*, 3569–3575.
(30) Lambert, T. N.; Chavez, C. A.; Hernandez-Sanchez, B.; Lu, P.; Bell, N. S.; Ambrosini, A.; Friedman, T.; Boyle, T. J.; Wheeler, D. R.; Huber, D. L. *J. Phys. Chem. C* **2009**, *113*, 19812–19823.
(31) Dreyer, D. R.; Park, S.; Bielawski, C. W.; Ruoff, R. S. *Chem. Soc. Rev.* **2010**, *39*, 228–240.
(32) Ge, J. P.; Hu, Y. X.; Biasini, M.; Beyermann, W. P.; Yin, Y. D. *Angew. Chem., Int. Ed.* **2007**, *46*, 4342–4345.
(33) Nethravathi, C.; Rajamathi, M. *Carbon* **2008**, *46*, 1994–1998.
(34) Teng, X. W.; Black, D.; Watkins, N. J.; Gao, Y. L.; Yang, H. *Nano Lett.* **2003**, *3*, 261–264.
(35) Morel, A. L.; Nikitenko, S. I.; Gionnet, K.; Wattiaux, A.; Lai-Kee-Him, J.; Labrugere, C.; Chevalier, B.; Deleris, G.; Petibois, C.; Brisson, A.; Simonoff, M. *ACS Nano* **2008**, *2*, 847–856.
(36) Ge, J. P.; Hu, Y. X.; Biasini, M.; Dong, C. L.; Guo, J. H.; Beyermann, W. P.; Yin, Y. D. *Chem.—Eur. J.* **2007**, *13*, 7153–7161.
(37) Sun, S. H.; Zeng, H.; Robinson, D. B.; Raoux, S.; Rice, P. M.; Wang, S. X.; Li, G. X. *J. Am. Chem. Soc.* **2004**, *126*, 273–279.
(38) Zhang, W. X.; Cui, J. C.; Tao, C. A.; Wu, Y. G.; Li, Z. P.; Ma, L.; Wen, Y. Q.; Li, G. T. *Angew. Chem., Int. Ed.* **2009**, *48*, 5864–5868.
(39) Stankovich, S.; Dikin, D. A.; Piner, R. D.; Kohlhaas, K. A.; Kleinhammes, A.; Jia, Y.; Wu, Y.; Nguyen, S. T.; Ruoff, R. S. *Carbon* **2007**, *45*, 1558–1565.
(40) Zhou, Y.; Bao, Q. L.; Tang, L. A. L.; Zhong, Y. L.; Loh, K. P. *Chem. Mater.* **2009**, *21*, 2950–2956.
(41) Williams, G.; Seger, B.; Kamat, P. V. *ACS Nano* **2008**, *2*, 1487–1491.
(42) Murray, C. B.; Kagan, C. R.; Bawendi, M. G. *Annu. Rev. Mater. Sci.* **2000**, *30*, 545–610.
(43) Yin, Y.; Alivisatos, A. P. *Nature* **2005**, *437*, 664–670.
(44) Wong, E. M.; Bonevich, J. E.; Searson, P. C. *J. Phys. Chem. B* **1998**, *102*, 7770–7775.
(45) Park, S.; An, J. H.; Jung, I. W.; Piner, R. D.; An, S. J.; Li, X. S.; Velamakanni, A.; Ruoff, R. S. *Nano Lett.* **2009**, *9*, 1593–1597.
(46) Li, D.; Muller, M. B.; Gilje, S.; Kaner, R. B.; Wallace, G. G. *Nat. Nanotechnol.* **2008**, *3*, 101–105.
(47) Ruoff, R. S. *Nat. Nanotechnol.* **2008**, *3*, 10–11.
(48) Gao, C.; Li, W.; Morimoto, H.; Nagaoka, Y.; Maekawa, T. *J. Phys. Chem. B* **2006**, *110*, 7213–7220.
(49) Terrones, M.; Grobert, N.; Olivares, J.; Zhang, J. P.; Terrones, H.; Kordatos, K.; Hsu, W. K.; Hare, J. P.; Townsend, P. D.; Prassides, K.; Cheetham, A. K.; Kroto, H. W.; Walton, D. R. M. *Nature* **1997**, *388*, 52–55.
(50) Stankovich, S.; Dikin, D. A.; Dommett, G. H. B.; Kohlhaas, K. M.; Zimney, E. J.; Stach, E. A.; Piner, R. D.; Nguyen, S. T.; Ruoff, R. S. *Nature* **2006**, *442*, 282–286.
(51) Qiu, G. H.; Wang, Q.; Nie, M. *J. Appl. Polym. Sci.* **2006**, *102*, 2107–2111.
(52) Gas, J.; Poddar, P.; Almand, J.; Srinath, S.; Srikanth, H. *Adv. Funct. Mater.* **2006**, *16*, 71–75.

AM100673G